



## Electronic structure of heterojunction MoO<sub>2</sub>/g-C<sub>3</sub>N<sub>4</sub> catalyst for oxidative desulfurization

Kun Chen<sup>a</sup>, Xiao-Min Zhang<sup>b</sup>, Xian-Feng Yang<sup>a</sup>, Meng-Gai Jiao<sup>a</sup>, Zhen Zhou<sup>a</sup>, Ming-Hui Zhang<sup>b,\*</sup>, Dan-Hong Wang<sup>a,\*</sup>, Xian-He Bu<sup>a,b</sup>

<sup>a</sup> TKL of Metal and Molecule Based Material Chemistry, National Institute for Advanced Materials, School of Materials Science and Engineering, Nankai University, Tianjin 300350, China

<sup>b</sup> Key Laboratory of Advanced Energy Materials Chemistry (Ministry of Education), College of Chemistry, Nankai University, Tianjin 300071, China



### ARTICLE INFO

#### Keywords:

MoO<sub>2</sub>  
g-C<sub>3</sub>N<sub>4</sub>  
heterojunction  
Electron transfer  
Oxidative desulfurization  
Mechanism

### ABSTRACT

Electronic structure of active sites plays a crucial role in redox catalysts. Herein, graphitic carbon nitride (g-C<sub>3</sub>N<sub>4</sub>) decorated with metallic MoO<sub>2</sub> heterojunction nanocomposites were successfully synthesized through a facile calcination route. XPS, UPS, UV-vis and PL spectra results suggest electron transfer from the conduction band (CB) of g-C<sub>3</sub>N<sub>4</sub> to unfilled  $\pi^*$  band of metallic MoO<sub>2</sub> in the metal-semiconductor heterojunction. The electron transfer ensures high intrinsic oxidative desulfurization activity for MoO<sub>2</sub>/g-C<sub>3</sub>N<sub>4</sub> composites. Radical scavenger experiments indicate that the electron transfer facilitates the enrichment of electron density around Mo active sites and control the rate-determining step of oxidative desulfurization. The approach can be extended to other low valent transition metal oxides possessing *d* electrons for enhanced catalytic activity in redox reactions.

### 1. Introduction

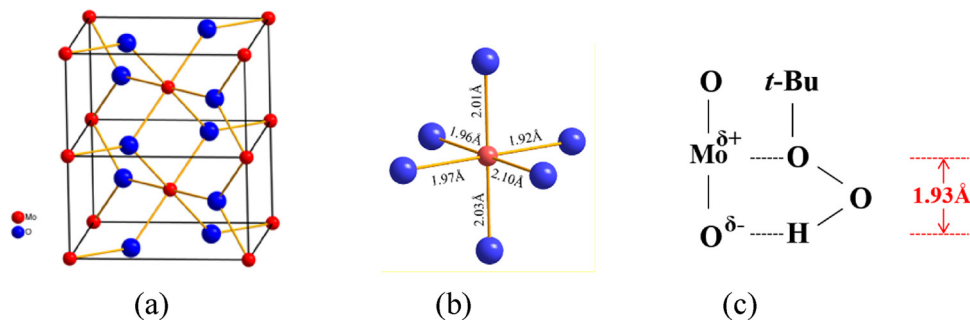
Sulfur contents in fuel oils have been restricted to ultra-low level (< 10 ppm) in many countries due to stringent environmental regulations [1]. The conventional hydrodesulfurization (HDS) process is widely applied to remove organosulfur compounds in petroleum hydrofining industry [2]. However, HDS is limited to eliminate refractory substituted dibenzothiophenes such as 4, 6-DMDBT (owing to steric hindrance) from oils. Oxidative desulfurization (ODS) has been regarded as a prospective and green technology for ultra-deep desulfurization due to its mild reaction conditions (room temperature and atmospheric pressure) and high efficiency. It is reported that highly substituted dibenzothiophenes can be most readily oxidized compared with thiophene by ODS reaction. [3,4].

In the past decade, many scientific research workers were looking forward to seeking a catalyst with an excellent performance on oxidation desulfurization. Several catalysts, such as metal oxides [3,5] or metal-based ionic liquid-supported catalysts [4,6], zeolites [7], metal-organic framework (MOF)-supported catalysts [8], and polyoxometalates [9], have been used to eliminate sulfur species from fuel oil. Among them, transition metal-based (Mo, W, Ti, V, etc.) materials are promising for the ultra-deep desulfurization of fuel oil under mild

conditions [10–12]. In particular, MoO<sub>3</sub> heterogeneous catalysts are reported to be remarkably successful for the ODS process. Many kinds of supports, such as titania, alumina, mesoporous silica, activated carbons and so on, have been generally used for preparation of supported MoO<sub>3</sub> catalysts. For example, Kabe and coauthors reported MoO<sub>3</sub> catalysts supported on Al<sub>2</sub>O<sub>3</sub> exhibit high activity in ODS with TBHP as oxidant [6]. Wang et al. investigated P-modified MoO<sub>3</sub>/SiO<sub>2</sub> catalysts with significant ODS performance [13]. MoO<sub>x</sub>-VO<sub>x</sub>/Al<sub>2</sub>O<sub>3</sub> and MoO<sub>x</sub>-VO<sub>x</sub> catalysts were synthesized for oxidative desulfurization and obtained desulfurization rate of 97% for DBT under the optimum reaction conditions [14]. We also reported that mesoporous SiM41C supported MoO<sub>3</sub> catalysts, which successfully reduced S content in a model fuel from 500 ppm to 0 ppm by ODS using TBHP as the oxidant [15]. To date, although many supports have been illustrated to be good for ODS, it is still a challenge to look for a new interesting support with high performance. Another extremely important point is the absence of systematic studies on the relationship between the catalytic efficiency and the catalyst structure, especially, the synergistic effect between the active sites and the supports. Rodriguez-Gattorno et al. investigated the origin of the acidity related to catalytic efficiency for WO<sub>x</sub>-ZrO<sub>2</sub> catalyst and found that the increase of Brønsted acidity density favored ODS activity [11]. Zhang et al. indicate that the oxidizability of tungstate

\* Corresponding authors.

E-mail addresses: [zhangmh@nankai.edu.cn](mailto:zhangmh@nankai.edu.cn) (M.-H. Zhang), [dhwang@nankai.edu.cn](mailto:dhwang@nankai.edu.cn) (D.-H. Wang).



**Scheme 1.** (a) distorted rutile structure of  $\text{MoO}_2$ . (b) bond lengths of distorted  $\text{MoO}_6$  octahedron in  $\text{MoO}_2$ . (c) the coordination of TBHP to Mo-O bond on  $\text{MoO}_2$ .

plays a synergistic role in activation of reactants and results in excellent ODS performance [4]. However, there are few studies focused on the electronic structures of ODS catalysts.

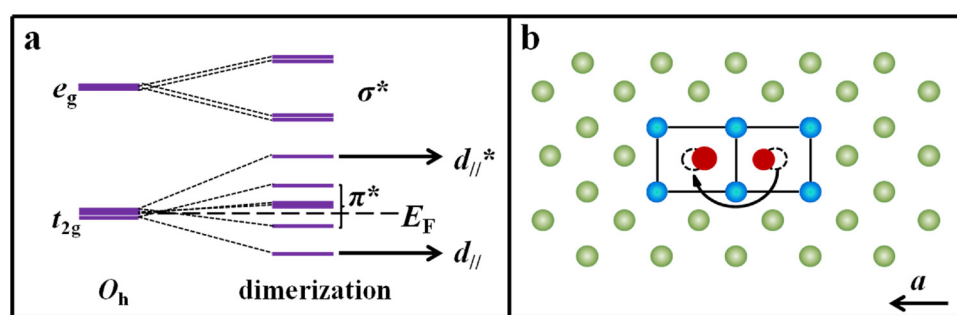
In our previous study [6,15],  $\text{MoO}_3$  catalyst presents high performance in ODS reaction with *tert*-butyl hydroperoxide (TBHP) as the oxidant and Mo-O bond acts as the active site. Mo-O bond lengths of  $\text{MoO}_6$  distorted octahedron in  $\text{MoO}_3$  orthorhombic crystal structure are 1.67, 1.73, 1.94, 1.94, 2.25, 2.33 Å [16]. Lower valent  $\text{MoO}_2$  can be easily obtained by the reduction of  $\text{MoO}_3$ . The monoclinic structure ( $P21/c$ ) for  $\text{MoO}_2$  crystal ( $a = 5.61$ ,  $b = 4.86$ ,  $c = 5.63$  Å,  $\beta = 121^\circ$ ,  $Z = 4$ ) is shown in Scheme 1a. In this distorted rutile structure with  $\text{MoO}_6$  distorted octahedron, two distinct Mo-Mo metal to metal bonds (2.51 and 3.10 Å) are formed, which causes two distinguishing oxygen coordination circumstances: (i) with Mo-O bond lengths of 1.92, 2.01 and 1.96 Å, (ii) with slightly longer Mo-O bond lengths of 1.97, 2.03 and 2.10 Å (Scheme 1b) [17]. Compared with  $\text{MoO}_3$ ,  $\text{MoO}_2$  shows appropriate Mo-O bond lengths for ODS reaction (Scheme 1c). The distance between the hydrogen atom and the peroxy oxygen atom neighboring to *tert*-butyl group is 1.93 Å, the coordination of peroxy O—O—H bonds to Mo-O bond on  $\text{MoO}_2$  constructs a five-member ring more easily than that on  $\text{MoO}_3$ , which is expected to enhance the oxidizability of the peroxy oxygen atom.

$\text{MoO}_2$  is less studied than  $\text{MoO}_3$ . Formally  $\text{MoO}_2$  is a  $4d^2$  Mo (IV) compound, which exhibits a metallic behavior [18]. The interpretation is that the Fermi level  $E_F$  of  $\text{MoO}_2$  is located within  $\text{Mo}_{4d}$  orbitals [19]. Usually,  $d$  orbitals of transition metal oxides separate into  $t_{2g}$  and  $e_g$  orbitals due to crystal field effect in octahedral ( $O_h$ ) symmetry. However, as shown in Scheme 2a, the  $x^2-y^2$  ( $t_{2g}$ ) orbital for  $\text{MoO}_2$  is divided into bonding ( $d_{//}$ ) and antibonding bands ( $d_{//}^*$ ) in virtue of paired Mo ions along monoclinic  $a$  axis (Scheme 2b). Other  $t_{2g}$  ( $xz, yz$ ) orbitals and  $e_g$  ( $z^2, xy$ ) orbitals show less influence by Mo dimerization (labeled as  $\pi^*$  and  $\sigma^*$  bands, respectively) [20]. As to the Fermi level  $E_F$  of  $\text{MoO}_2$ , according to ultraviolet photoelectron spectroscopy (UPS) measurements and density-functional-theory (DFT) calculations, two  $\text{Mo}_{4d}$  bands just lie below the Fermi level: at  $\sim 0.5$  and  $\sim 1.5$  eV in experiment and at  $\sim 0.3$  and  $\sim 1.5$  eV in theory [17,21,22].  $d_{//}$  band below Fermi level is fully occupied.  $\pi^*$  band around Fermi level can hold four

electrons per  $\text{Mo}^{4+}$  cation. However, only one extra electron per  $\text{Mo}^{4+}$  cation is possessed in the lowest energy band of  $\pi^*$  band, the  $\pi^*$  band around Fermi level is less than half-full. As a result  $\text{MoO}_2$  presents metallic conductivity by metal-metal bonding. The  $\text{Mo}_{4d}$  bands around Fermi level will take part in redox processes.

Recently, graphitic carbon nitride ( $\text{g-C}_3\text{N}_4$ ) attracts many interests for its good photocatalytic activity and moderate band gap energy ( $E_g$ ) as a semiconductor [23].  $\text{g-C}_3\text{N}_4$  shows two-dimensional structure with N-bridged tri-s-triazine repeating units [24]. DFT calculations indicate the band gap in the melem molecule is 2.67 eV, which is supported by the ultraviolet-visible experiments [25,26]. The valence band (VB) for the melem molecule is a combination of the highest occupied molecular orbital (HOMO) levels, which are donated by nitrogen  $p_z$  orbitals. The conduction band (CB) for the melem molecule can be related to the lowest unoccupied molecular orbital (LUMO) levels, which mainly consist of carbon  $p_z$  orbitals [23]. Carbon atom in the melem molecule presents  $sp^2$  hybridization, and each carbon atom possesses one free electron in carbon  $p_z$  orbitals. Recent studies show that coating  $\text{MoO}_3$  with  $\text{g-C}_3\text{N}_4$  decreases the electron-hole recombination and obtains enhanced efficiency of photocatalysts [27–29]. However, there are relatively few studies devoted to low valent  $\text{MoO}_2/\text{g-C}_3\text{N}_4$  catalyst.

As expected,  $\text{MoO}_2$  shows appropriate Mo-O bond lengths for ODS reaction, the electrons in  $\text{Mo}_{4d}$  bands around Fermi level will have an effect on redox processes. Moreover, the electrons in carbon  $p_z$  orbitals of  $\text{g-C}_3\text{N}_4$  will also play some important roles due to the combination of metallic  $\text{MoO}_2$  and semiconducting  $\text{g-C}_3\text{N}_4$ . In this work, a facile route to synthesize a series of  $\text{MoO}_2/\text{g-C}_3\text{N}_4$  metal-semiconductor heterojunction composites is developed and such heterojunction composites show remarkably enhanced ODS activity. Owing to that the electronic structure of  $\text{MoO}_2/\text{g-C}_3\text{N}_4$  is very important and has not yet been understood, the nature of synergic effect between  $\text{MoO}_2$  and  $\text{g-C}_3\text{N}_4$  is clearly elucidated and the ODS mechanism is further discussed in this paper.



**Scheme 2.** (a) crystal field effect on  $\text{Mo}_{4d}$  levels for Mo-Mo dimerization. (b) Mo-Mo bonding along monoclinic  $a$  axis, red and blue circles represent molybdenum and oxygen ions [20].

## 2. Experimental

### 2.1. Catalyst preparation

According to the previous research [30], the bulk g-C<sub>3</sub>N<sub>4</sub> powders were prepared by calcination of melamine. 10 g melamine was placed in a 50 ml crucible with cover, then heated by a rate of 3 °C/min using muffle furnace and kept for 2 h at 550 °C. Yellow products were obtained and then milled for 15 min.

MoO<sub>2</sub>/g-C<sub>3</sub>N<sub>4</sub> catalyst was synthesized by impregnation method together with ultrasonic-assisted dispersion. A certain amount of g-C<sub>3</sub>N<sub>4</sub> powder and calculated amount of (NH<sub>4</sub>)<sub>6</sub>Mo<sub>7</sub>O<sub>24</sub>·4H<sub>2</sub>O (equal to 20 wt % MoO<sub>2</sub>) were added into 60 ml distilled water under stirring for 1 h, followed by ultrasonic agitation for 0.5 h, then dried with rotary evaporation at 70 °C. The obtained precursor powder was ground and placed in a quartz boat, then heated at different temperatures (450, 500, 550 and 600 °C) for 2 h with a rate of 5 °C/min under nitrogen atmosphere. The corresponding catalysts were marked as MoO<sub>2</sub>/g-C<sub>3</sub>N<sub>4</sub>-x, where x means the calcination temperature under nitrogen atmosphere.

### 2.2. Catalyst characterization

X-ray diffraction (XRD) spectra of the catalysts were characterized by a Rigaku D/Max-2500 equipped with a Cu-target tube and scanned by a rate of 6.0°/min over the 2θ range of 10°–80°. Fourier transform infrared (FTIR) spectra were performed on a Bruker TENSOR 37. The morphology of the catalysts was examined by HRTEM and EDX (Philips Tecnai G2 F20 microscope). Thermogravimetric analysis (TG) is used to determine the real content of MoO<sub>2</sub> in the composites by a TA SDT Q600 instrument. X-ray photoelectron spectroscopy (XPS) and ultra-violet photoelectron spectroscopy (UPS) were operated on a Thermo Scientific ESCALAB 250Xi using excitation photon energy (1486.6 eV) for XPS and He I ( $\hbar\nu = 21.22$  eV) as the exciting source for UPS. Surface areas were calculated using N<sub>2</sub> adsorption/desorption BET method conducted at 77 K with a BELSORP-mini II sorption apparatus. The UV-vis diffused reflectance spectra (DRS) of the catalysts were carried out by a TU-1950 spectrophotometer. Photoluminescence spectra (PL) of the catalysts were tested on an F-7000 spectrometer, using a Xe lamp (350 nm) as light source.

### 2.3. Catalytic reaction

The as-prepared MoO<sub>2</sub>/g-C<sub>3</sub>N<sub>4</sub> catalysts were tested for oxidative desulfurization of DBT using a batch reactor. A simulated diesel oil (500 ppm DBT) was prepared as following: a solution of 500 mg/g of DBT was obtained by dissolving 0.05 g DBT in 99.95 g decalin. 0.1141 g tert-butyl hydroperoxide (TBHP) was then added in the DBT solution with the O/S molar ratio of 3.0 (moles of oxygen atom in TBHP/moles of sulfur atom in DBT). In a typical ODS procedure, 10 g simulated diesel oil in a 50 ml round bottom flask was heated to 80 °C under stirring, then 0.05 g catalyst was mixed and the ODS reaction lasted for 2 h. During the oxidation, the reaction products were detected every 10 min using a gas chromatograph (GC 2060) equipped with an FID.

### 2.3. Theoretical calculation methods

First-principles computations were performed through the density functional theory (DFT) as implemented in the Vienna ab initio simulation package (VASP) [31]. Projector augmented wave (PAW) based potentials were used to describe nuclei-electron interactions [32]. The Perdew-Burke-Ernzerhof form of the Generalized-Gradient Approximation was employed to describe electron exchange and correlation [33]. The wave functions at each k-point were expanded with a plane wave basis set and a kinetic cutoff energy up to 400 eV. The integration of the Brillouin zone was conducted using 2 × 3 × 1 Monkhorst-Pack

grids [34]. The electron occupancies were determined using Fermi broadening with a width of 0.1 eV. All geometries were fully relaxed and optimized until the energy was converged to  $1.0 \times 10^{-5}$  eV per atom and the force was converged to 0.05 eV/Å. DFT-D3 method with Becke-Jonson damping was applied to describe the van der Waals interactions [35,36]. The reaction pathways and energy barriers were calculated by the climbing-image nudged elastic band (CI-NEB) method [37]. The energy barrier ( $E$ ) was defined as  $E = E_{TS} - E_{IS}$  and the reaction energy ( $\Delta E$ ) was calculated from the equation  $\Delta E = E_{FS} - E_{IS}$ , where  $E_{IS}$ ,  $E_{TS}$  and  $E_{FS}$  are the energy of the initial, transition and final state, respectively. According to this definition, the negative and positive values represent exothermic and endothermic reactions, respectively. The MoO<sub>2</sub> (011) surface was modeled with a 2 × 1 supercell, built from the optimized MoO<sub>2</sub> primitive cell. A vacuum space larger than 15 Å was inserted in the z direction to prevent interactions between periodically.

## 3. Results and discussion

### 3.1. Characterization of MoO<sub>2</sub>/g-C<sub>3</sub>N<sub>4</sub> catalysts

Fig. 1 shows XRD patterns of MoO<sub>2</sub>/g-C<sub>3</sub>N<sub>4</sub> catalysts calcined at different temperatures in nitrogen atmosphere. MoO<sub>2</sub>/g-C<sub>3</sub>N<sub>4</sub> composites can be obtained at 450, 500, 550 °C. The diffraction peaks of both g-C<sub>3</sub>N<sub>4</sub> and MoO<sub>2</sub> can be observed in the obtained MoO<sub>2</sub>/g-C<sub>3</sub>N<sub>4</sub> composites, confirming the coexistence of g-C<sub>3</sub>N<sub>4</sub> and MoO<sub>2</sub> [24,38]. It is obvious that the peak of g-C<sub>3</sub>N<sub>4</sub> decreases with increasing calcination temperature up to 550 °C and disappears at 600 °C. Pure MoO<sub>2</sub> is obtained at 600 °C. These results can be interpreted with the decomposition of g-C<sub>3</sub>N<sub>4</sub> at higher temperature. FTIR analysis (Fig. S1) further confirms that g-C<sub>3</sub>N<sub>4</sub> maintains tri-s-triazine structure in the obtained MoO<sub>2</sub>/g-C<sub>3</sub>N<sub>4</sub> composites [39].

TG was carried out in air atmosphere to determine the real content of MoO<sub>2</sub> in as-synthesized MoO<sub>2</sub>/g-C<sub>3</sub>N<sub>4</sub> catalysts (Fig. 2). Pure g-C<sub>3</sub>N<sub>4</sub> begins to decompose at temperature above 520 °C, while for MoO<sub>2</sub>/g-C<sub>3</sub>N<sub>4</sub> composites, the beginning of mass-loss shift to 420 °C. This result suggests that MoO<sub>2</sub> promotes the combustion of g-C<sub>3</sub>N<sub>4</sub>, which is confirmed by DSC results (Fig. S2), implying the synergic effect between MoO<sub>2</sub> and g-C<sub>3</sub>N<sub>4</sub>. Similar results are reported for MoO<sub>3</sub>/g-C<sub>3</sub>N<sub>4</sub>, CeO<sub>2</sub>/g-C<sub>3</sub>N<sub>4</sub> and V<sub>2</sub>O<sub>5</sub>/g-C<sub>3</sub>N<sub>4</sub> catalysts [29,40–42]. The gaining weight up to 350 °C for MoO<sub>2</sub>/g-C<sub>3</sub>N<sub>4</sub>-600 (pure MoO<sub>2</sub>) are matched well with the mass of MoO<sub>2</sub> oxidization to MoO<sub>3</sub>, which is confirmed by XRD results. The real content of MoO<sub>2</sub> in MoO<sub>2</sub>/g-C<sub>3</sub>N<sub>4</sub> composites can be estimated

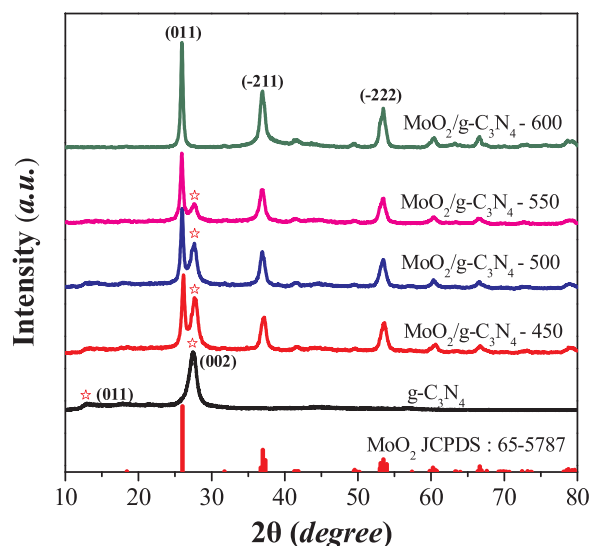


Fig. 1. XRD patterns of MoO<sub>2</sub>/g-C<sub>3</sub>N<sub>4</sub> catalysts obtained at different calcination temperatures (450, 500, 550 and 600 °C).

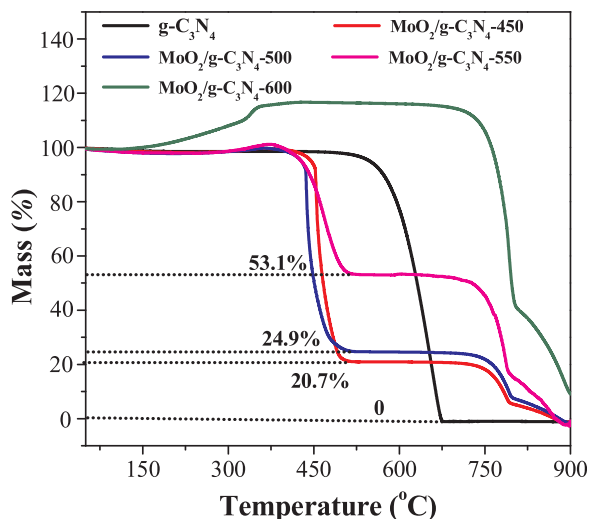


Fig. 2. TG curves in air atmosphere for as-synthesized MoO<sub>2</sub>/g-C<sub>3</sub>N<sub>4</sub> catalysts.

**Table 1**  
Specific surface area, pore volume and MoO<sub>2</sub> content of as-synthesized catalysts.

Sample	Surface area (m <sup>2</sup> /g)	Pore Volume (cm <sup>3</sup> /g)	MoO <sub>2</sub> content per mass%
g-C <sub>3</sub> N <sub>4</sub>	11	0.0834	0
MoO <sub>2</sub> /g-C <sub>3</sub> N <sub>4</sub> - 450	40	0.2431	18.9
MoO <sub>2</sub> /g-C <sub>3</sub> N <sub>4</sub> - 500	55	0.3432	22.7
MoO <sub>2</sub> /g-C <sub>3</sub> N <sub>4</sub> - 550	77	0.5394	50.2
MoO <sub>2</sub> /g-C <sub>3</sub> N <sub>4</sub> - 600	9	0.0997	100

from the remaining MoO<sub>3</sub> mass after heating above 600°C (Table 1). The weight loss above 750 °C is attributed to the sublimation of MoO<sub>3</sub> [29]. TG of the catalyst precursor was carried out in nitrogen atmosphere to determine the decomposition temperature during the catalyst preparation (Fig. S3). The results of XRD, FTIR and TG indicate that MoO<sub>2</sub>/g-C<sub>3</sub>N<sub>4</sub> composites with different MoO<sub>2</sub> content (19–50 wt%) have been successfully synthesized.

The nitrogen adsorption-desorption curves of the catalysts are displayed in Fig. S4. The BET surface areas of synthesized MoO<sub>2</sub>/g-C<sub>3</sub>N<sub>4</sub> catalysts are listed in Table 1. With an increase in the calcination temperature up to 550 °C, both surface area and pore volume of the catalysts increase, and MoO<sub>2</sub> loading also increases. MoO<sub>2</sub>/g-C<sub>3</sub>N<sub>4</sub>-600 shows lowest surface area and pore volume which is attributed to the formation of pure bulk MoO<sub>2</sub> (g-C<sub>3</sub>N<sub>4</sub> decomposed completely).

The morphological features of pure g-C<sub>3</sub>N<sub>4</sub> and MoO<sub>2</sub>/g-C<sub>3</sub>N<sub>4</sub> composites were examined by TEM. Pure g-C<sub>3</sub>N<sub>4</sub> (Fig. 3a) appears to be a lamellar structure, which the monolayer surface is very smooth. With increasing Mo contents in MoO<sub>2</sub>/g-C<sub>3</sub>N<sub>4</sub>-450, -500 and -550 samples (Fig. 3b-d), some monolayer-dispersed MoO<sub>2</sub> clusters together in bulk MoO<sub>2</sub>. Despite high MoO<sub>2</sub> content (50 wt%) in MoO<sub>2</sub>/g-C<sub>3</sub>N<sub>4</sub>-550 sample, most of MoO<sub>2</sub> are well-dispersed on the lamellas of g-C<sub>3</sub>N<sub>4</sub> nanosheets except for some bulk MoO<sub>2</sub> marked by red ring in Fig. 3d. A clear lattice fringe of 0.3447 nm is observed for the bulk MoO<sub>2</sub> by HRTEM image in Fig. 3e, which is consistent with the interplanar spacing of (011) plane (JCPDS 65–5787,  $d_{011} = 0.3423$  nm) [38]. It is demonstrated that MoO<sub>2</sub>/g-C<sub>3</sub>N<sub>4</sub> composites are formed by the coupling of MoO<sub>2</sub> {011} crystal planes and g-C<sub>3</sub>N<sub>4</sub> sheets. MoO<sub>2</sub>/g-C<sub>3</sub>N<sub>4</sub>-600 sample (Fig. 3f) presents to be pure MoO<sub>2</sub> according to the interplanar spacing of the clusters. EDX spectrum (Fig. 3g) confirms that MoO<sub>2</sub>/g-C<sub>3</sub>N<sub>4</sub>-550 sample includes C, N, Mo and O elements. Elemental mapping analyses (Fig. 3h-m) of N element (green) and Mo element (red) for MoO<sub>2</sub>/g-C<sub>3</sub>N<sub>4</sub> composites give the results that MoO<sub>2</sub> is well-dispersed on g-C<sub>3</sub>N<sub>4</sub> nanosheets. Further, with increasing Mo contents

in MoO<sub>2</sub>/g-C<sub>3</sub>N<sub>4</sub> composites the dispersion degree of MoO<sub>2</sub> decreases. Based on the above results, the well dispersed MoO<sub>2</sub> enables more intimate contact with g-C<sub>3</sub>N<sub>4</sub> for synergistic effect compared with the bulk MoO<sub>2</sub> as shown in Scheme 3. MoO<sub>2</sub>/g-C<sub>3</sub>N<sub>4</sub>-450 sample is suggested to allow highly dispersed MoO<sub>2</sub> on g-C<sub>3</sub>N<sub>4</sub> due to its low Mo loading and low calcination temperature compared with MoO<sub>2</sub>/g-C<sub>3</sub>N<sub>4</sub>-500 and -550 samples.

XPS analysis was performed to determine the surface electronic structure of MoO<sub>2</sub>/g-C<sub>3</sub>N<sub>4</sub> catalysts calcined at different temperatures. XPS spectra are shown in Fig. 4 and peak fitting results are shown in Fig. S5. From Fig. 4a, at the binding energies of 284.8 and 288.1 eV, two C1s peaks are observed for g-C<sub>3</sub>N<sub>4</sub> and MoO<sub>2</sub>/g-C<sub>3</sub>N<sub>4</sub> catalysts except MoO<sub>2</sub>/g-C<sub>3</sub>N<sub>4</sub>-600. The peak at 284.8 eV ascribes to sp<sup>2</sup> C-C bonds of diffused MoO<sub>2</sub> as standard binding energy. The peak at 288.1 eV corresponds to N–C = N bonds in the tri-azine rings of g-C<sub>3</sub>N<sub>4</sub> [43]. MoO<sub>2</sub>/g-C<sub>3</sub>N<sub>4</sub>-600 sample (pure MoO<sub>2</sub>) has no peaks at 288.1 eV, which reveals no existence of g-C<sub>3</sub>N<sub>4</sub>. C1s peaks at 288.1 eV for MoO<sub>2</sub>/g-C<sub>3</sub>N<sub>4</sub> composites shift to high binding energies compared with that of pure g-C<sub>3</sub>N<sub>4</sub>, suggesting strong interaction between the tri-azine rings and MoO<sub>2</sub>. In Fig. 4b, N1s spectrum of pure g-C<sub>3</sub>N<sub>4</sub> can be deconvoluted into three peaks located at 398.6 eV, 399.6 eV and 401.1 eV (Fig. S5), which are equivalent to pyridinic-N species, N atoms trigonal-bonding with sp<sup>2</sup> or sp<sup>3</sup> carbon atoms, terminal amino-groups (-NH<sub>2</sub>), respectively [44]. The main N1s peak at 398.6 eV for MoO<sub>2</sub>/g-C<sub>3</sub>N<sub>4</sub> composites shift to high binding energies compared with that of pure g-C<sub>3</sub>N<sub>4</sub>, which also means the strong synergistic effect between g-C<sub>3</sub>N<sub>4</sub> and MoO<sub>2</sub>. The peak at about 397 eV for MoO<sub>2</sub>/g-C<sub>3</sub>N<sub>4</sub> composites suggests the formation of Mo-N bond and the peak at around 395.5 eV belongs to Mo3p<sub>3/2</sub> (Fig. S5) [45]. O1s spectra are displayed in Fig. 4c. MoO<sub>2</sub>/g-C<sub>3</sub>N<sub>4</sub>-600 sample (pure MoO<sub>2</sub>) shows a strong O1s peak at 530.7 eV which can be assigned to the O<sup>2-</sup> in MoO<sub>2</sub>. The O1s peaks for MoO<sub>2</sub>/g-C<sub>3</sub>N<sub>4</sub> composites locate at about 530.1 eV and shift to low binding energy compared with that of pure MoO<sub>2</sub>, implying that MoO<sub>2</sub> interacts with g-C<sub>3</sub>N<sub>4</sub>. Mo3d peaks are shown in Fig. 4d. The binding energies of Mo<sup>4+</sup> (3d<sub>5/2</sub>, 3d<sub>3/2</sub>) lie at around 229.7 and 232.9 eV, the binding energies of Mo<sup>6+</sup> (3d<sub>5/2</sub>, 3d<sub>3/2</sub>) lie at 232.6 and 235.9 eV (Fig. S5) [29,46]. Partial surface Mo<sup>4+</sup> chemical state of MoO<sub>2</sub> is oxidized to Mo<sup>5+</sup> and Mo<sup>6+</sup> due to the absorption of oxygen and hydroxyl groups. Compared with Mo3d binding energies of pure MoO<sub>2</sub>, all the Mo3d peaks of MoO<sub>2</sub>/g-C<sub>3</sub>N<sub>4</sub> composites shift to low binding energies, and the amounts of Mo<sup>4+</sup> species are also enhanced, giving clear evidences that electron transfer occurs from g-C<sub>3</sub>N<sub>4</sub> to MoO<sub>2</sub>.

As obtained above, comparing MoO<sub>2</sub>/g-C<sub>3</sub>N<sub>4</sub> composites with pure g-C<sub>3</sub>N<sub>4</sub>, C1s and N1s binding energies increase, while O1s and Mo3d binding energies decrease. This result clearly indicates the transference of electron from g-C<sub>3</sub>N<sub>4</sub> nanosheets to well-dispersed MoO<sub>2</sub> nanoparticles, which will benefit the formation of heterojunction structure by combining MoO<sub>2</sub> with g-C<sub>3</sub>N<sub>4</sub>.

Fig. 5a shows the results of UV-vis diffuse reflectance spectra. Pure g-C<sub>3</sub>N<sub>4</sub> exhibits a sharp absorption edge at 470 nm identical to 2.64 eV. MoO<sub>2</sub>/g-C<sub>3</sub>N<sub>4</sub> heterojunction composites present obvious red-shifts of the absorption edges due to the presence of metallic MoO<sub>2</sub>. The background absorption for MoO<sub>2</sub>/g-C<sub>3</sub>N<sub>4</sub> composites is stronger than that for pure g-C<sub>3</sub>N<sub>4</sub>, which can be explained by the fact that the colors change from yellow to dark grey. Band gap energies of the as-synthesized composites are illustrated in Fig. 5b. Using the following equation,  $E_g$  of a semiconductor can be calculated:

$$c\hbar\nu = A(\hbar\nu - E_g)^{n/2}$$

Here  $E_g$ ,  $\alpha$ ,  $h$ ,  $\nu$  and  $A$  represent band gap energy, absorption coefficient, Planck constant, photon frequency and a constant, respectively.  $n$  is 1 for direct gap semiconductor and  $n$  is 4 for indirect gap semiconductor. According to the plot of  $\ln(\alpha h\nu) \sim \ln(h\nu - E_g)$  for g-C<sub>3</sub>N<sub>4</sub> in this work,  $n/2$  can be calculated from the slope to be 2 ( $n = 4$ ), gives the evidence that g-C<sub>3</sub>N<sub>4</sub> presents as an indirect band gap. This result is very consistent

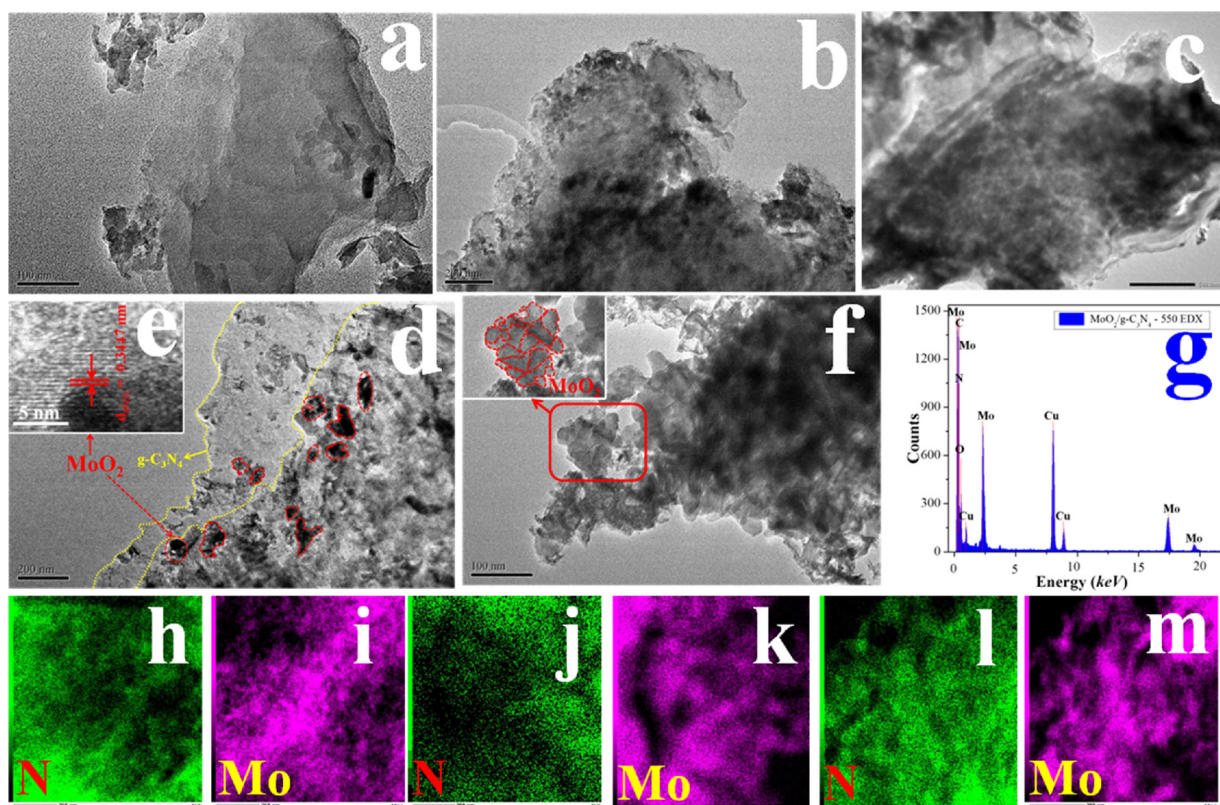
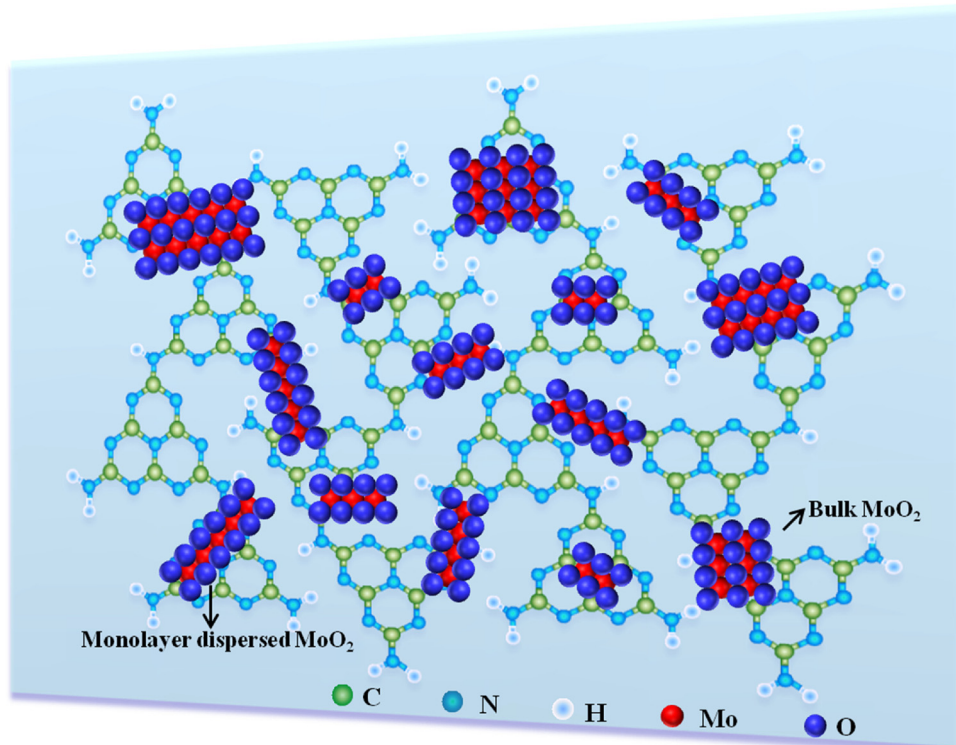


**Fig. 3.** (a) TEM image of pure g-C<sub>3</sub>N<sub>4</sub> (b) TEM image of MoO<sub>2</sub>/g-C<sub>3</sub>N<sub>4</sub>-450 (c) TEM image of MoO<sub>2</sub>/g-C<sub>3</sub>N<sub>4</sub>-500 (d) TEM image of MoO<sub>2</sub>/g-C<sub>3</sub>N<sub>4</sub>-550 (e) HRTEM image of MoO<sub>2</sub>/g-C<sub>3</sub>N<sub>4</sub>-550 (f) TEM image of MoO<sub>2</sub>/g-C<sub>3</sub>N<sub>4</sub>-600 (g) EDX spectrum of MoO<sub>2</sub>/g-C<sub>3</sub>N<sub>4</sub>-550 (h,i) elemental mapping images of MoO<sub>2</sub>/g-C<sub>3</sub>N<sub>4</sub>-450. (j,k) elemental mapping images of MoO<sub>2</sub>/g-C<sub>3</sub>N<sub>4</sub>-500. (l,m) elemental mapping images of MoO<sub>2</sub>/g-C<sub>3</sub>N<sub>4</sub>-550.



**Scheme 3.** Monolayer-dispersed MoO<sub>2</sub> and bulk MoO<sub>2</sub> on g-C<sub>3</sub>N<sub>4</sub> nanosheet.

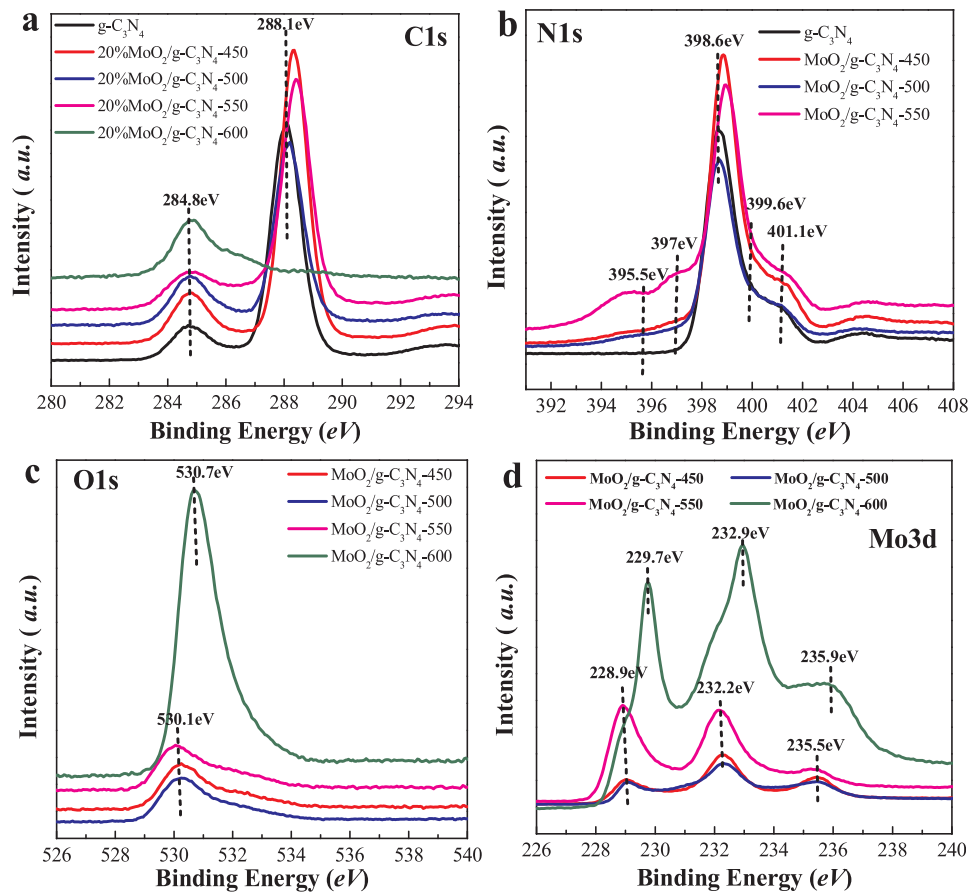


**Fig. 4.** XPS spectra of  $\text{MoO}_2/\text{g-C}_3\text{N}_4$  catalysts (a)C1s, (b) N1s, (c) O1s, (d) Mo3d.

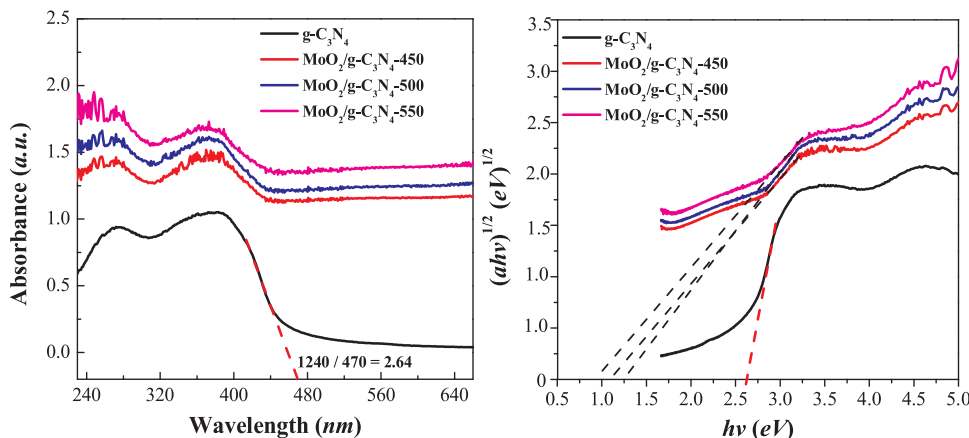
with the reported results according to UV-vis experiments [47] and DFT calculations [48]. Therefore in Fig. 5b,  $E_g$  of  $\text{g-C}_3\text{N}_4$  is calculated to be 2.64 eV from a plot of  $(ahv)^{1/2} \sim h\nu$ , which is very close to the reported 2.67 eV [47]. The most interesting result is that the introducing of  $\text{MoO}_2$  into  $\text{g-C}_3\text{N}_4$  brings about a significant decrease in the band gap to 1.0–1.2 eV for  $\text{MoO}_2/\text{g-C}_3\text{N}_4$  composites, which clearly suggests the formation of heterojunction between metallic  $\text{MoO}_2$  and semiconducting  $\text{g-C}_3\text{N}_4$ .

The Photoluminescence spectra of pure  $\text{g-C}_3\text{N}_4$  and  $\text{MoO}_2/\text{g-C}_3\text{N}_4$  composites are shown in Fig. 6. Pure  $\text{g-C}_3\text{N}_4$  exhibits strong PL intensity at about 470 nm, which means a prompt recombination of electrons in CB and holes in VB. The PL result is in good accordance with the band

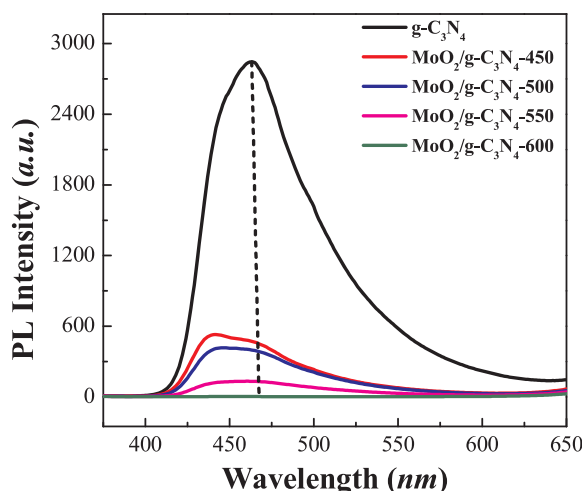
gap (2.64 eV) obtained from UV-vis spectra. With an increase in  $\text{MoO}_2$  content for  $\text{MoO}_2/\text{g-C}_3\text{N}_4$  composites the PL emission intensity at 470 nm decreases sharply.  $\text{MoO}_2/\text{g-C}_3\text{N}_4$ -600 (pure  $\text{MoO}_2$ ) shows no PL emission. The fact that the fluorescence of  $\text{MoO}_2/\text{g-C}_3\text{N}_4$  composite is obviously quenched verifies the existence of electron transfer from semiconducting  $\text{g-C}_3\text{N}_4$  to metallic  $\text{MoO}_2$  particles.

### 3.2. Evaluation of oxidative desulfurization activities

ODS activities of the as-synthesized  $\text{MoO}_2/\text{g-C}_3\text{N}_4$  catalysts were examined via the oxidation of DBT using TBHP as the oxidant. The ODS experiments excluded the internal and external diffusion of the catalysts

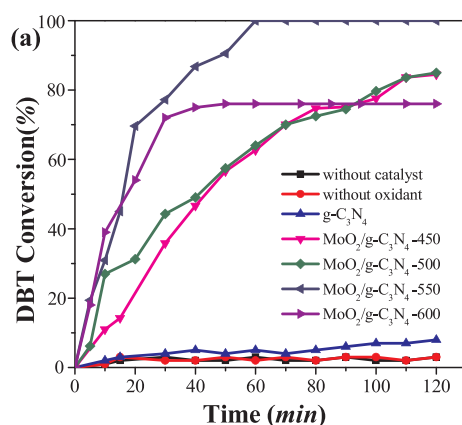


**Fig. 5.** (a) UV-vis diffuse reflection spectra of pure  $\text{g-C}_3\text{N}_4$  and  $\text{MoO}_2/\text{g-C}_3\text{N}_4$  composites (b) Plots of the  $(ahv)^{1/2}$  vs. photon energy for pure  $\text{g-C}_3\text{N}_4$  and  $\text{MoO}_2/\text{g-C}_3\text{N}_4$  composites.

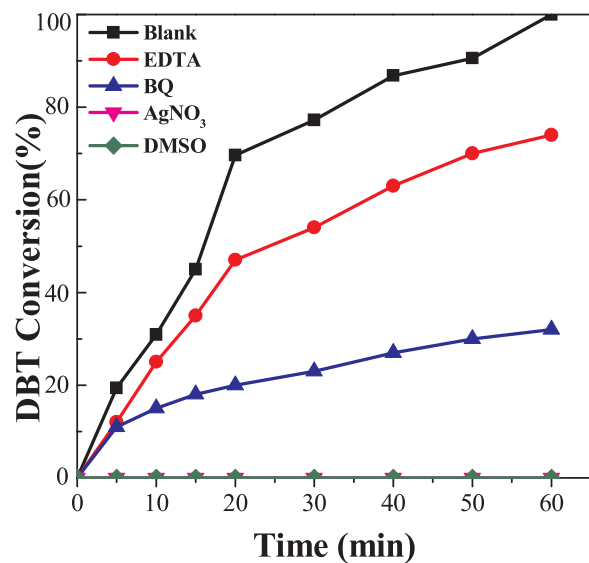


**Fig. 6.** Photoluminescence spectra of pure  $\text{g-C}_3\text{N}_4$  and  $\text{MoO}_2/\text{g-C}_3\text{N}_4$  composites.

by reducing the particles size (grinded to  $> 200$  mesh) and increasing the reaction stirring speed. Fig. 7 shows the ODS results over the catalysts. The oxidation of DBT will not occur without catalyst or oxidant. With increasing  $\text{MoO}_2$  contents in  $\text{MoO}_2/\text{g-C}_3\text{N}_4$  composites, the ODS activities increase. It is apparent that  $\text{MoO}_2/\text{g-C}_3\text{N}_4$ -550 catalyst exhibits excellent desulfurization performance which can successfully eliminate sulfur content to 0 ppm after 60 min's reaction. This result would be attributed to higher Mo loadings and more active sites for  $\text{MoO}_2/\text{g-C}_3\text{N}_4$ -550 catalyst. Therefore, to compare the intrinsic activity for  $\text{MoO}_2/\text{g-C}_3\text{N}_4$  composites, TON value is defined and calculated according to the formula of  $\text{TON} = n/m$  ( $n$  is the mole of reacted DBT per gram catalyst,  $m$  is the mole of surface  $\text{MoO}_2$  per gram catalyst). In the monoclinic  $\text{MoO}_2$  ( $P21/c$ ) crystal structure, each  $\text{MoO}_2$  molecule occupies a volume of  $32.9 \text{ \AA}^3$ , equivalent to an effective area of  $10.2 \text{ \AA}^2$ . Therefore, the mole of surface  $\text{MoO}_2$  can be calculated from the surface area of the  $\text{MoO}_2/\text{g-C}_3\text{N}_4$  catalysts, assuming that the surfaces of the catalysts are completely covered by  $\text{MoO}_2$  molecules. With increasing calcination temperatures and  $\text{MoO}_2$  loadings, the TON values for  $\text{MoO}_2/\text{g-C}_3\text{N}_4$  composites decrease.  $\text{MoO}_2/\text{g-C}_3\text{N}_4$ -450 sample shows the highest TON values, suggesting that the synergistic effect between  $\text{MoO}_2$  and  $\text{g-C}_3\text{N}_4$  with low Mo loading favors the ODS activity. As obtained by TEM results,  $\text{MoO}_2$  presents the highest dispersion on  $\text{g-C}_3\text{N}_4$  for  $\text{MoO}_2/\text{g-C}_3\text{N}_4$ -450 sample, implying that well-dispersed  $\text{MoO}_2$  on  $\text{g-C}_3\text{N}_4$  displays higher intrinsic ODS activity than bulk  $\text{MoO}_2$  on  $\text{g-C}_3\text{N}_4$ . Therefore, the more effective electron transfer from  $\text{g-C}_3\text{N}_4$  to well-dispersed  $\text{MoO}_2$  offers the guarantee of higher electron density on



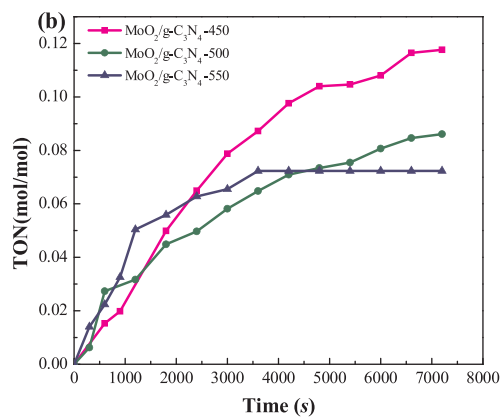
**Fig. 7.** (a) ODS activities over  $\text{g-C}_3\text{N}_4$  and  $\text{MoO}_2/\text{g-C}_3\text{N}_4$  catalysts. (b) Calculated TON values for  $\text{MoO}_2/\text{g-C}_3\text{N}_4$  catalysts. Reaction conditions: 10 g simulated diesel oil, 0.05 g catalyst, 353 K, O/S = 3:1.



**Fig. 8.** ODS activities over  $\text{MoO}_2/\text{g-C}_3\text{N}_4$ -550 catalyst with different scavengers. Reaction conditions: 60 min, 10 g simulated diesel oil, 0.05 g catalyst, 353 K, O/S = 3:1.

Mo active sites, which makes it possible to achieve higher intrinsic ODS activity.

In order to elucidate ODS reaction mechanism and the main reactive species, dimethyl sulfoxide (DMSO), ethylene diamine tetraacetic acid (EDTA) and p-benzoquinone (BQ) were used respectively as the scavengers for hydroxyl radicals ( $\cdot\text{OH}$ ), holes ( $\text{h}^+$ ) and superoxide radicals ( $\cdot\text{O}_2^-$ ) [42,49]. Further,  $\text{AgNO}_3$  aqueous solution is used as the scavenger for electrons ( $\text{e}^-$ ). The results are shown in Fig. 8. All scavengers were added with excessive quantities (0.1 mmol, about 3 equivalent amounts of DBT). Compared with the blank scavenger-free experiment, the oxidation rate of DBT is inhibited slightly (15%) by the addition of EDTA, implying that holes ( $\text{h}^+$ ) present as less important reactive species during ODS reaction. The addition of BQ severely inhibited the oxidation rate of DBT (62%), indicating  $\cdot\text{O}_2^-$  radicals present as an important reactive species during ODS reaction. It is noteworthy that the addition of  $\text{AgNO}_3$  aqueous solution and DMSO shows absolute inhibition effect on ODS reaction, which suggests that electrons ( $\text{e}^-$ ) and hydroxyl radicals present as the most important reactive species during ODS reaction. The possibilities of  $\text{AgNO}_3$  aqueous solution or DMSO reacting with the oxidant TBHP are eliminated by the blank DBT-free experiments (There is no Ag precipitate observed or DMSO remains itself according to GC analysis). Thus, the  $\cdot\text{OH}$  hydroxyl radicals and  $\text{e}^-$  electrons are proved to be the major active species for



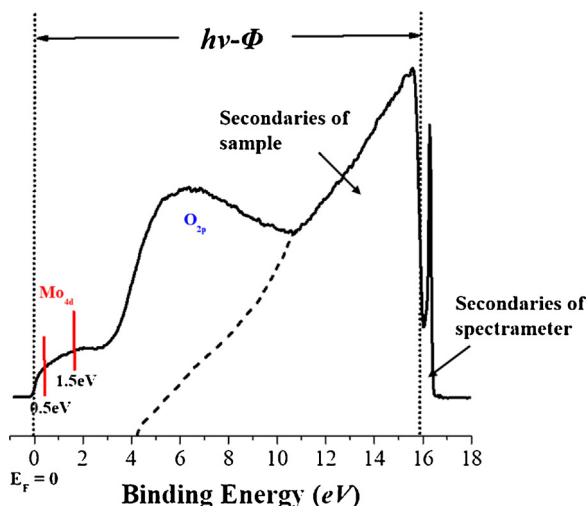


Fig. 9. UPS He I photoemission spectrum ( $h\nu = 21.2$  eV) of  $\text{MoO}_2$ .

ODS reaction on  $\text{MoO}_2/\text{g-C}_3\text{N}_4$  catalyst.

### 3.3. Electronic structure of $\text{MoO}_2/\text{g-C}_3\text{N}_4$ composites

The electronic structure of pure  $\text{MoO}_2$  is determined by UPS He I ( $h\nu = 21.2$  eV) photoemission spectra (Fig. 9). In the spectra at low binding energy (0.5 and 1.5 eV) two peaks are found to be assigned to  $\text{Mo}_{4d}$  states, which are incorporated into a broad band ascribed to  $\text{O}_{2p}$  states.  $\text{O}_{2p}$  band successively incorporates into the peak attributed to secondary electron emission.  $d$  band at higher binding energy of 1.5 eV is appointed to  $d_{\parallel}$  band, and  $d$  band at lower binding energy of 0.5 eV is owing to  $\pi^*$  band as discussed in Scheme 2a. A significant decline in density of states at the Fermi level is observed in Fig. 9, suggesting that  $\text{MoO}_2$  remains metallic character. The work function ( $\Phi$ ) of  $\text{MoO}_2$ , defined to be the energy difference between the Fermi level and the vacuum level, is calculated by subtracting the incident He I photon energy from the energy extent of UPS spectrum when secondary electron emission of the sample is terminated ( $21.2-15.9 = 5.3$  eV). Therefore, the Fermi level of  $\text{MoO}_2$  relative to the vacuum level is -5.3 eV. The two  $\text{Mo}_{4d}$  peaks of  $\text{MoO}_2$  just below Fermi level at ~0.5 and ~1.5 eV are also reported by other researchers [50,51].

As  $\text{MoO}_2$  is expected for a metallic compound, DFT calculations are further performed to determine the electronic band structure and the wave functions. As shown in Fig. 10 a distinct metallic band structure is confirmed for the monoclinic  $\text{MoO}_2$  ( $P21/c$ ). The strong Mo-Mo dimerization discussed in Introduction results in the metallic behavior. The electronic density of states for  $\text{MoO}_2$  are shown in Fig. 11. The

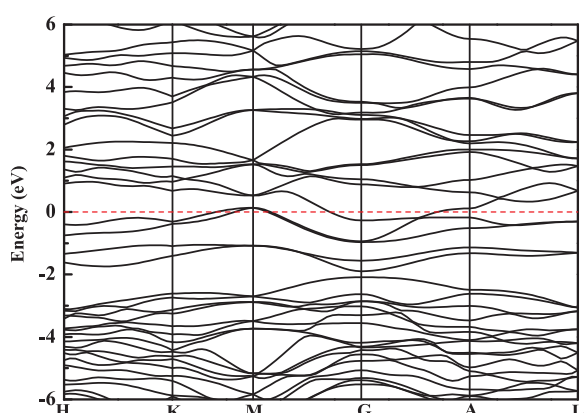


Fig. 10. Electronic band structure along the high-symmetry points for  $\text{MoO}_2$ . The dashed line denotes the Fermi energy.

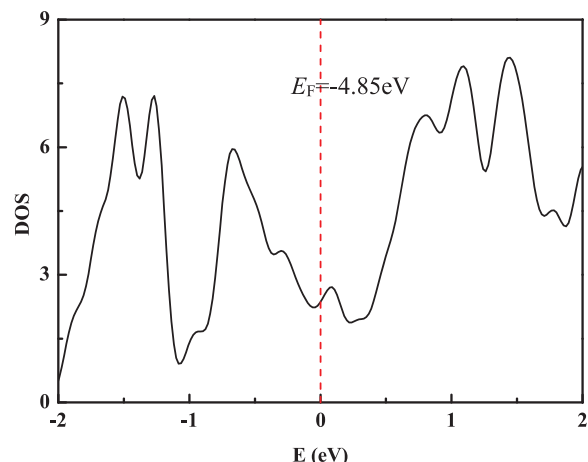


Fig. 11. Total electronic density of states for  $\text{MoO}_2$ . The dashed line denotes the Fermi energy.

electronic structure close to the  $E_F$  is mainly contributed by  $\text{Mo}_{4d}$  character, which comprises two peaks at ~0.5 and ~1.5 eV below the Fermi energy ( $E_F = -4.85$  eV). These results fit well with our UPS results and other reported theoretical DFT calculation results. [50,51].

To elucidate the nature of enhanced catalytic activity on  $\text{MoO}_2/\text{g-C}_3\text{N}_4$  composite, the VB and CB potentials of  $\text{g-C}_3\text{N}_4$  vs SHE were calculated using the following formula:

$$E_{CB} = X - E^e - 1/2E_g$$

$$E_{VB} = E_{CB} + E_g$$

$X$  is the electronegativity of  $\text{g-C}_3\text{N}_4$  (4.73 eV) [52].  $E^e$  is the energy of standard hydrogen electrode relevant to vacuum level ( $E^e = 4.5$  eV).  $E_g$  is the band gap energy of  $\text{g-C}_3\text{N}_4$  (2.64 eV). From the calculation, the  $E_{CB}$  of  $\text{g-C}_3\text{N}_4$  is about -1.10 vs. SHE, and the  $E_{VB}$  of  $\text{g-C}_3\text{N}_4$  is estimated to be 1.54 vs. SHE. Fig. 12 shows the electronic structure of  $\text{MoO}_2/\text{g-C}_3\text{N}_4$  metal-semiconductor heterojunction. As obtained by UPS results, the Fermi level of  $\text{MoO}_2$  is -5.3 eV, then the Fermi level vs. SHE is calculated to be  $-(5.3)-4.5 = 0.8$ . The excited thermoelectrons in the conduction band (carbon  $p_z$  orbitals containing free electrons) of  $\text{g-C}_3\text{N}_4$  are easily transferred to the LUMO of  $\text{Mo}_{4d}$  band (unfilled  $\pi^*$  band, 0.5 eV below the Fermi level) of  $\text{MoO}_2$ , a Schottky juction is then formed. The electron transfer inhibits the recombination of electrons in CB and holes in VB for  $\text{g-C}_3\text{N}_4$ , which leads to fluorescence quenching in PL spectra (Fig. 6). The electron transfer also results in high electron density on Mo (IV) active sites which may play an important role in ODS mechanism.

### 3.4. ODS mechanism on $\text{MoO}_2/\text{g-C}_3\text{N}_4$ composites

We also make some meaningful attempt to understand the ODS mechanism on  $\text{MoO}_2$  composites. Based on Mashio's research [53] and Kropp's research [54], we proposed the possible ODS mechanisms of DBT on  $\text{MoO}_2$  with TBHP. Mashio et al. supposed that the five-member ring is formed through the coordination of *tert*-butyl hydroperoxide to Mo-O. Kropp et al. suggested that surface silanol groups of silica performed as the catalytic active sites to form a five-member ring with TBHP through hydrogen bonding.

Consequently, on the basis of the electronic structure of  $\text{MoO}_2/\text{g-C}_3\text{N}_4$  composite and the radical scavenger experiments, the most probable ODS mechanism is bring forward as shown in Scheme 4 when hydroxyl radicals and electrons act as the main reactive species. First, the chemisorption of TBHP on Mo-O active site leads to the formation of a coordinated five-member ring. Particularly, high electron density of Mo atom in  $\text{MoO}_2/\text{g-C}_3\text{N}_4$  composite facilitates the chemisorption of peroxy O atom with Mo atom. The electron scavengers  $\text{AgNO}_3$

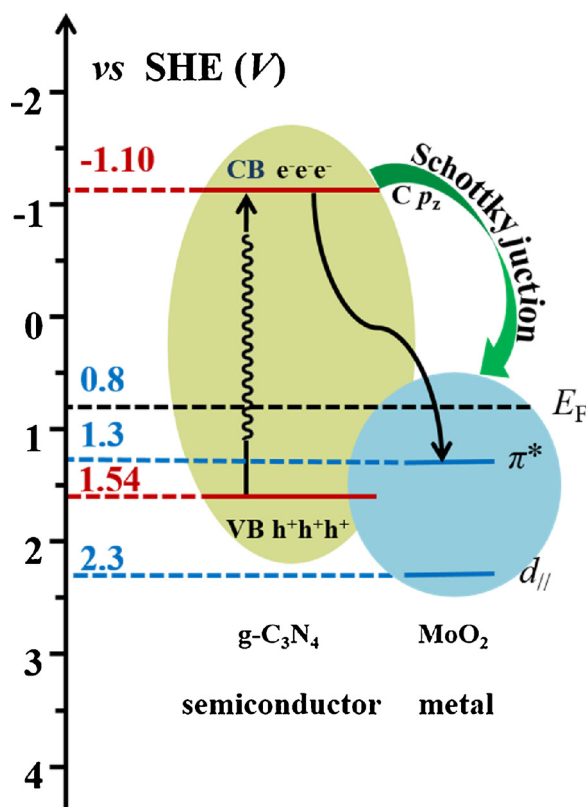


**Fig. 12.** The electronic structure of  $\text{MoO}_2/\text{g-C}_3\text{N}_4$  metal-semiconductor heterojunction.

absolutely inhibit the ODS reaction, giving the evidence that electron transfer is the most important step. In step 1, attributing to high electron density on Mo atom (some electrons transferred from  $\text{g-C}_3\text{N}_4$ ), electron transfer will easily occur from Mo to neighboring  $\text{O}_2$  atom. High electron density on  $\text{O}_2$  atom brings about easier  $\text{O}-\text{O}$  bond cleavage, which leads to the formation of  $\cdot\text{OH}$  radicals. In step 2, the formed  $\cdot\text{OH}$  radicals show high oxidizability, the sulfur atom of DBT then nucleophilic attacks the specific  $\text{O}_1$  atom leading to the formation

of sulfoxide. Therefore, step 1 including electron transfer and  $\text{O}-\text{O}$  bond cleavage acts as the rate-determining step.

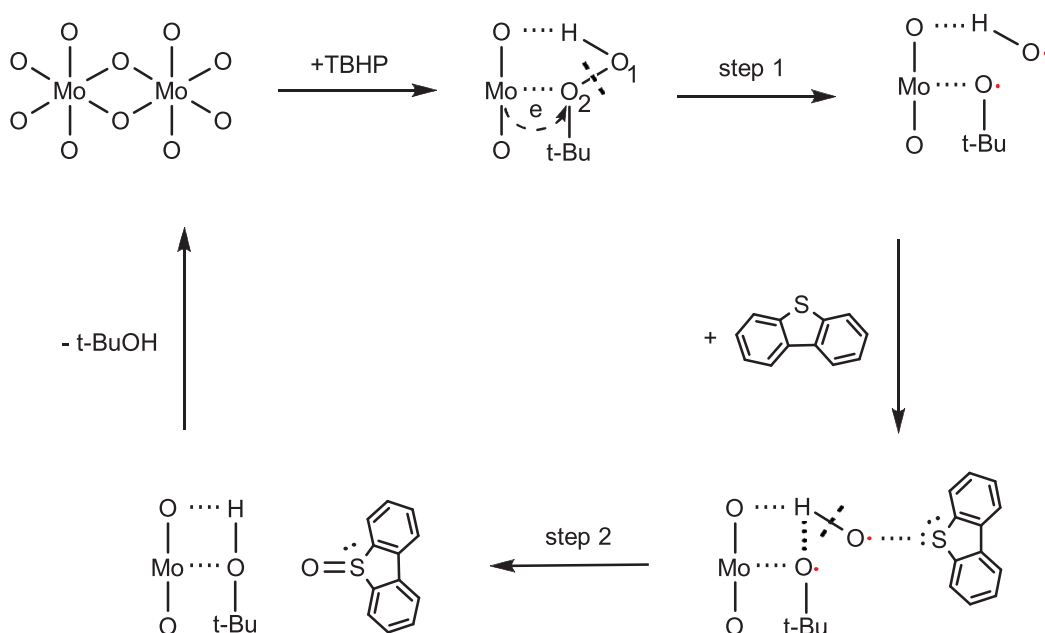
BQ shows an inhibition effect of 61% on the ODS reaction, implying that  $\cdot\text{O}_2^-$  may also present as a reactive species. So another possible ODS mechanism is shown in **Scheme 5**. In step 1  $\text{O}-\text{H}$  bond cleavage is suggested to happen instead of  $\text{O}-\text{O}$  bond cleavage. Tert butyl cation with relative stability may also be formed, then superoxide radicals is produced in this step.  $\cdot\text{O}_2^-$  presents high oxidizability which can oxidize the sulfur atom in DBT easily.

To further investigate the feasibility of the above two reaction pathways, the energy barriers were calculated by the CI-NEB method. To simplify the calculation, model molecule of hydrogen peroxide is used as a substitute for TBHP oxidant. As shown in **Fig. 13**, the ODS reaction on  $\text{MoO}_2$  experiences the five-member ring transition state. When  $\text{O}-\text{O}$  bond cleavage leads to the formation of hydroxyl radicals ( $\cdot\text{OH}$ ), the activation energy of the reaction is only required to be 0.24 eV and the reaction is exothermic. When the cleavage of  $\text{H}-\text{O}$  bond to form  $\cdot\text{OOH}$  radicals is required, the activation energy of the reaction is 2.68 eV and the reaction is endothermic. Thus, hydroxyl radical is suggested to be more easily formed on  $\text{MoO}_2$  in ODS reaction.

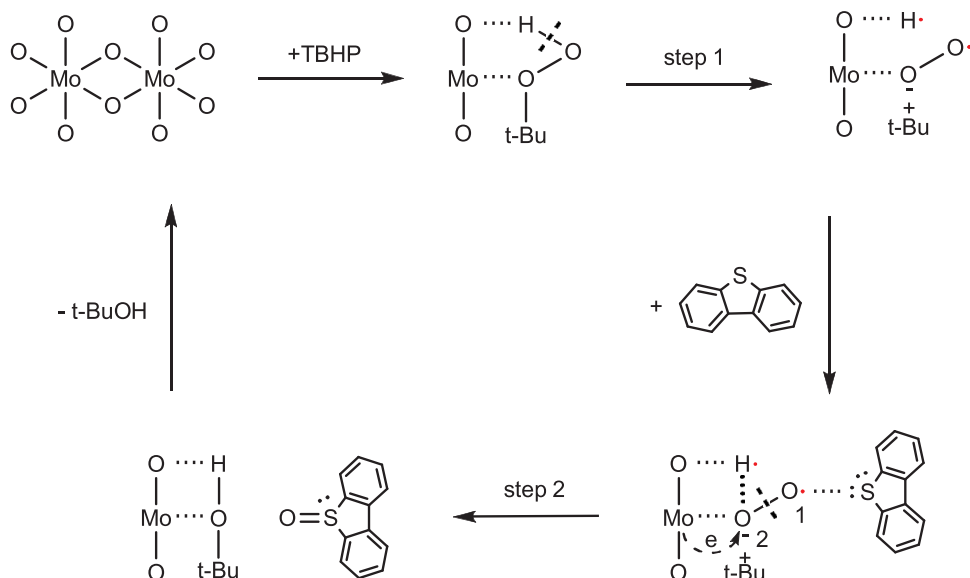
#### 4. Conclusions

In summary, we present here  $\text{MoO}_2/\text{g-C}_3\text{N}_4$  as a metal-semiconductor heterojunction. The nature of synergic effect between  $\text{MoO}_2$  and  $\text{g-C}_3\text{N}_4$  is particularly elucidated.

- (1)  $\text{MoO}_2/\text{g-C}_3\text{N}_4$  composites with different  $\text{MoO}_2$  contents (19–50 wt %) have been successfully synthesized by a facile calcination method.
- (2) XPS results clearly indicate that electron transfer from  $\text{g-C}_3\text{N}_4$  to  $\text{MoO}_2$  occurs for  $\text{MoO}_2/\text{g-C}_3\text{N}_4$  heterojunction composite.
- (3) Through UV-vis results, the introducing of  $\text{MoO}_2$  into  $\text{g-C}_3\text{N}_4$  decreases the band gap from 2.64 eV of  $\text{g-C}_3\text{N}_4$  to 1.0–1.2 eV of  $\text{MoO}_2/\text{g-C}_3\text{N}_4$ , which indicates the metallic character of  $\text{MoO}_2$ .
- (4) According to UPS results, a significant decline in density of states at the Fermi level ( $E_F = -5.3$  eV) is observed for pure  $\text{MoO}_2$ , suggesting that  $\text{MoO}_2$  presents metallic character.
- (5) The electron transfer from the valence band of  $\text{g-C}_3\text{N}_4$  to unfilled  $\text{Mo}_{4d}$  band of  $\text{MoO}_2$  prevents the recombination of electrons and



**Scheme 4.** The most probable ODS mechanism of  $\text{t-BuO}_2\text{H} \rightarrow \text{t-BuO}\cdot + \cdot\text{OH}$  on  $\text{MoO}_2/\text{g-C}_3\text{N}_4$  catalyst.



**Scheme 5.** Another possible ODS mechanism of  $t\text{-BuO}_2\text{H} \rightarrow t\text{-Bu}^+ + \text{O}_2^- + \cdot\text{H}$  on  $\text{MoO}_2/\text{g-C}_3\text{N}_4$  catalyst.

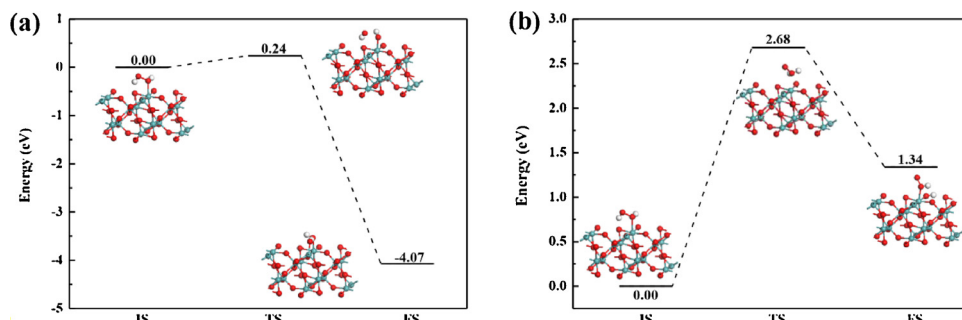


**Fig. 13.** Reaction pathway of dissociation of  $\text{H}_2\text{O}_2$  on  $\text{MoO}_2$  (011): (a)  $\text{H}_2\text{O}_2 \rightarrow \text{HO}\cdot + \cdot\text{OH}$  (b)  $\text{H}_2\text{O}_2 \rightarrow \text{HOO}\cdot + \cdot\text{H}$ .

- holes, which leads to fluorescence quenching in PL spectra. The electron transfer also results in high electron density on Mo atom and a Schottky juction is then formed.
- (6) Hydroxyl radicals and  $e^-$  electrons are proved to be the major reactive species for ODS reaction on  $\text{MoO}_2/\text{g-C}_3\text{N}_4$  composite.
  - (7) Well-dispersed  $\text{MoO}_2$  on  $\text{g-C}_3\text{N}_4$  displays higher intrinsic ODS activity than bulk  $\text{MoO}_2$  on  $\text{g-C}_3\text{N}_4$  due to the higher electron density of Mo active sites.
  - (8) High electron density of Mo atom for  $\text{MoO}_2/\text{g-C}_3\text{N}_4$  composite facilitates O–O bond cleavage, which is responsible for the rate-determining step in ODS reaction.
  - (9) Theoretical calculations indicate that  $\text{MoO}_2$  presents metallic band structure and hydroxyl radical is easily formed on  $\text{MoO}_2$  in ODS reaction.

The present results open new vistas for redox reaction using metal-semiconductor structures as the functional catalyst.

#### Acknowledgments

This work was partly supported by National Natural Science Foundation of China (21421001, 21576140 and 21703107), Natural Science Foundation of Tianjin city (17JCYBJC20000 and 14JCYBJC20000), the Fundamental Research Funds for the Central Universities (63185015), Postdoctoral Fund Project (2016M601254) and MOE innovation Team (IRT13R30 and IRT13022) of China.

#### Appendix A. Supplementary data

Supplementary material related to this article can be found, in the online version, at doi:<https://doi.org/10.1016/j.apcatb.2018.07.037>.

#### References

- [1] J. Eßler, P. Wasserscheid, A. Jess, Green Chem. 6 (2004) 316–322.
- [2] D.H. Wang, W.H. Qian, A. Ishihara, T. Kabe, J. Catal. 209 (2002) 266–270.
- [3] K. Chen, N. Liu, M.H. Zhang, D.H. Wang, Appl. Catal. B 212 (2017) 32–40.
- [4] B.Y. Zhang, Z.X. Jiang, J. Li, Y.N. Zhang, F. Lin, Y. Liu, C. Li, J. Catal. 287 (2012) 5–12.
- [5] X. Xiao, H. Zhong, C.X. Zheng, M.L. Lu, X.X. Zuo, J.M. Nan, Chem. Eng. J. 304 (2016) 908–916.
- [6] D.H. Wang, E.W.H. Qian, H. Amano, K. Okata, A. Ishihara, T. Kabe, Appl. Catal. A. 253 (2003) 91–99.
- [7] Q. Du, Y.P. Guo, H.N. Duan, H. Li, Y.J. Chen, H.Z. Liu, Fuel Lond. (Lond.) 188 (2017) 232–238.
- [8] P. Tan, X.Y. Xie, X.Q. Liu, T. Pan, C. Gu, P.F. Chen, J.Y. Zhou, Y.C. Pan, L.B. Sun, J. Hazard. Mater. 321 (2017) 344–352.
- [9] B. Bertleff, J. Claußnitzer, W. Korth, P. Wasserscheid, A. Jess, J. Albert, ACS Sustain. Chem. Eng. 5 (2017) 4110–4118.
- [10] E. Torres-García, A. Galano, G. Rodríguez-Gattorno, J. Catal. 282 (2011) 201–208.
- [11] G. Rodríguez-Gattorno, A. Galano, E. Torres-Garcíá, Appl. Catal. B 92 (2009) 1–8.
- [12] Y.H. Jia, G. Li, G.L. Ning, Fuel Process. Technol. 92 (2011) 106–111.
- [13] X.H. Han, A.J. Wang, X.S. Wang, X. Li, Y. Wang, Y.K. Hu, Catal. Commun. 42 (2013) 6–9.
- [14] M.A. Alvarez-Amparan, L. Ceden o-Caero, Catal. Today 282 (2017) 133–139.
- [15] D.H. Wang, N. Liu, J.Y. Zhang, X. Zhao, W.H. Zhang, M.H. Zhang, J. Mol. J. Mol. Catal. A. Chem. 393 (2014) 47–55.
- [16] D.O. Scanlon, G.W. Watson, D.J. Payne, G.R. Atkinson, R.G. Egdel, D.S.L. Law, J. Biophys. Biochem. Cytol. 114 (2010) 4636–4645.
- [17] R. Tokarz-Sobieraj, R. Grybos, M. Witko, Appl. Catal. A. 391 (2011) 137–143.
- [18] Z.C. Xiang, Q. Zhang, Z. Zhang, X.J. Xua, Q.B. Wang, Ceram. Int. 41 (2015) 977–981.

- [19] K. Inzani, M. Nematollahi, F. Vullum-Bruer, T. Grande, T.W. Reenaas, S.M. Selbach, *Phys. Chem. Chem. Phys.* 19 (2017) 9232–9245.
- [20] V. Stoeberl, M. Abbate, L.M.S. Alves, C.A.M. dos Santos, R.J.O. Mossanek, *J. Alloy. Compnd.* 691 (2017) 138–143.
- [21] H. Al-Kandaria, A.M. Al-Kandarib, F. Mohameda, A. Al-Kharafia, Katriba, *Appl. Biocatal. Biotransform.* 475 (2014) 497–502.
- [22] A. Gulino, T.S. Parker, F.H. Jones, R.G. Egdell, *J. Chem. Soc. Faraday Trans.* 92 (12) (1996) 2137–2141.
- [23] X.C. Wang, K. Maeda, A. Thomas, K. Takanabe, G. Xin, J.M. Carlsson, K. Domen, M. Antonietti, *Nat. Mater.* 8 (2009) 76–80.
- [24] F.K. Kessler, Y. Zheng, D. Schwarz, C. Merschjann, W. Schnick, X.C. Wang, M.J. Bojdys, *Nat. Rev. Mater.* 2 (2017) 17030.
- [25] K. Maeda, X.C. Wang, Y. Nishihara, D.L. Lu, M. Antonietti, K. Domen, *J. Biophys. Biochem. Cytol.* 113 (2009) 4940–4947.
- [26] D.L. Jiang, J.J. Zhu, M. Chen, J.M. Xie, *J. Colloid Interface Sci.* 417 (2014) 115–120.
- [27] L.Y. Huang, H. Xua, R.X. Zhang, X.N. Cheng, J.X. Xia, Y.G. Xu, H.M. Li, *Appl. Surf. Sci.* 283 (2013) 25–32.
- [28] Y.P. Li, L.Y. Huang, J.B. Xu, H. Xu, Y.G. Xu, J.X. Xia, H.M. Li, *Mater. Res. Bull.* 70 (2015) 500–505.
- [29] Y.M. He, L.H. Zhang, X.X. Wang, Y. Wu, H.J. Lin, L.H. Zhao, W.Z. Weng, H.L. Wan, M.H. Fan, *RSC Adv.* 4 (2014) 13610–13619.
- [30] J. Su, X.X. Zou, G.D. Li, X. Wei, C. Yan, Y.N. Wang, J. Zhao, L.J. Zhou, J.S. Chen, *J. Phys. Chem. C* 115 (2011) 8064–8071.
- [31] G. Kresse, J. Furthmüller, *Phys. Rev. B* 54 (16) (1996) 11169–11186.
- [32] G. Kresse, D. Joubert, *Phys. Rev. B* 59 (3) (1999) 1758–1775.
- [33] J.P. Perdew, K. Burke, M. Ernzerhof, Generalized gradient approximation made simple, *Phys. Rev. lett.* 77 (18) (1996) 3865–3868.
- [34] H.J. Monkhorst, J.D. Pack, *Phys. Rev. B* 13 (12) (1976) 5188–5192.
- [35] S. Grimme, J. Antony, S. Ehrlich, H. Krieg, *J. Chem. Phys.* 132 (15) (2010) 154104.
- [36] S. Grimme, S. Ehrlich, L. Goerigk, *J. Comput. Chem.* 32 (7) (2011) 1456–1465.
- [37] G. Henkelman, H. Jónsson, *J. Chem. Phys.* 113 (22) (2000) 9978–9985.
- [38] Q.W. Tang, Z.Q. Shan, L. Wang, X. Qin, *Electrochim. Acta* 79 (2012) 148–153.
- [39] X.P. Song, Q. Yang, X.H. Jiang, M.Y. Yin, L.M. Zhou, *Appl. Catal. B* 217 (2017) 322–330.
- [40] L.H. Tana, J.H. Xua, X.J. Zhang, Z.S. Hang, Y.Q. Jia, S.B. Wang, *Appl. Surf. Sci.* 356 (2015) 447–453.
- [41] Q.Q. Liu, C.Y. Fan, H. Tang, X.J. Sun, J. Yang, X.N. Cheng, *Appl. Surf. Sci.* 358 (2015) 188–195.
- [42] J. Ding, Q.Q. Liu, Z.Y. Zhang, X. Liu, J.Q. Zhao, S.B. Cheng, B.N. Zong, W.L. Dai, *Appl. Catal. B* 165 (2015) 511–518.
- [43] G.T.S.T. da Silva, K.T.G. Carvalho, O.F. Lopes, C. Ribeiro, *Appl. Catal. B* 216 (2017) 70–79.
- [44] J. Ding, Q.Q. Liu, Z.Y. Zhang, X. Liu, J.Q. Zhao, S.B. Cheng, B.N. Zong, W.L. Dai, *Appl. Catal. B* 165 (2015) 511–518.
- [45] T. Wang, G.J. Zhang, S. Ren, B.L. Jiang, *J. Alloys* 701 (2017) 1–8.
- [46] J.S. Li, Y. Wang, C.H. Liu, S.L. Li, Y.G. Wang, L.Z. Dong, Z.H. Dai, Y.F. Li, Y.Q. Lan, *Nat. Commun.* 7 (2016) 11204.
- [47] Y. Di, M. Antonietti, H.R. Li, X.F. Chen, X.C. Wang, *Chem. Mater.* 22 (2010) 18.
- [48] Y. Xu, S.P. Gao, *Int. J. Hydrogen Energy* 37 (2012) 11072–11080.
- [49] S. Fukui, Y. Hanasaki, S. Ogawa, *Chinese J. Chromatogr.* 630 (1993) 187–193.
- [50] R. Tokarz-Sobieraj, R. Grybo's, M. Witko, *Appl. Catal. A* 391 (2011) 137–143.
- [51] O. Marin-Flores, L. Scudiero, S. Ha, *Surf. Sci.* 603 (2009) 2327–2332.
- [52] A. Gulino, T.S. Parker, F.H. Jones, R.G. Egdell, *J. Chem. Soc. Faraday Trans.* 92 (12) (1996) 2137–2141.
- [53] F. Mashio, S. Kato, Yuki Gousei Kagaku. 26 (4) (1968) 367.
- [54] P.J. Kropp, G.W. Breton, J.D. Fields, J.C. Tung, B.R. Loomis, *J. Am. Chem. Soc.* 122 (2000) 4280–4284.